MATERIALS CHEMISTRY FRONTIERS

RESEARCH ARTICLE

View Article Online
View Journal | View Issue

Cite this: *Mater. Chem. Front.*, 2025, **9**, 1690

Direct styrene hydrogenation on a metal-free boron–nitrogen doped carbon catalyst†

Neeraj Gupta, *[a] Abhishek Soni,[a] Sahil Kumar,[b] Mamta Shandilya,[b] Elisabetta Inico,[c] Ilaria Barlocco,[d] Giovanni Di Liberto *[c] and Alberto Villa *[d]

Received 17th December 2024,
Accepted 3rd April 2025

DOI: 10.1039/d4qm01107d

rsc.li/frontiers-materials

We present a study of direct styrene hydrogenation to ethylbenzene by a metal-free catalyst. The catalyst is a nanohybrid made up of ultra-dispersed diamond (UDD) and graphitic sheets. The method to prepare the catalyst introduces the key active site (bearing B and N atoms) into the sp^2 rich layer over the surface of UDD. The results show excellent catalytic activity for the direct hydrogenation of styrene to ethylbenzene in the presence of isopropyl alcohol, where hydrogen comes directly from the oxidation of the alcohol to acetone. The combination of experimental characterization and quantum chemical simulation indicates that a key role is played by direct B═N bonds and pyrrolic-N is the most probable active site in the reaction.

1. Introduction

Catalytic hydrogenation of organic compounds containing unsaturated bonds has drawn comprehensive attention since the early 20th century. The hydrogenation of unsaturated bonds is very crucial due to their atom economy, the cleanliness of the transformation and its ubiquitous presence in industrial processes.[1] Alkenes serve as a valuable feedstock and central intermediates in chemical, pharmaceutical, petrochemical and material industries. Indeed, a variety of bulk and fine chemicals as well as chemicals derived from renewable sources contain C═C bonds.[2] The catalyst-based olefin hydrogenation typically relies on precious metals like palladium,[3] platinum,[4] ruthenium,[5] rhodium[6] and iridium.[7] Two major disadvantages associated with the use of these metals include their high cost and risk of leaching into the products.[8] Despite the variety of hydrogenation methods, a greener and sustainable metal-free catalytic system to achieve efficient hydrogenation using safe and straightforward reaction conditions is highly desirable.[9] Various metal-free catalysts, including frustrated Lewis pairs (FLPs),[10] organocatalysts[11,12] and carbon-based catalysts[13–15] have been employed for the hydrogenation of olefins, offering eco-friendly and versatile alternatives to traditional metal catalysts.

The carbon materials like carbon nanotubes,[13] graphene,[14,15] graphitic carbon nitrides,[16] activated carbon[17] and carbon-supported metal catalysts[18,19] provide diverse choices for catalyzing olefin hydrogenation reactions. The FLPs contain Lewis acids (B compounds) and Lewis bases (P/N compounds) that cannot combine to form a classical adduct due to steric hindrance, offering a way to activate H_2 and other small molecules (*e.g.* alkenes and alkynes; CO_2 and other oxides of p-block; acidic and hydridic N–H/H–H bonds).[20–22] The traditional FLPs are effective in hydrogenation and the bulky substituents are crucial to prevent the formation of Lewis acid–base adducts.[23] Direct hydrogenation with H_2 gas and a transfer hydrogenation process are the two strategies commonly employed for the hydrogenation process. The transfer hydrogenation refers to the addition of hydrogen to a molecule using a hydrogen source other than H_2 gas. It is an attractive alternative to direct hydrogenation, and it has recently become the center of research in hydrogenation science.[24]

Deng Sheng Su *et al.* carried out the hydrogenation of olefins by using electron-rich nitrogen and electron-deficient boron-doped ultra-dispersed diamond (UDD) in the presence of H_2 gas.[25] We have previously achieved the catalytic hydrogenation of styrene by using a carbon-based catalyst rich in –B═N– moieties, in the presence of H_2 gas.[16] The UDDs are known for their exceptional properties, like good thermal conductivity, non-toxicity, tunable surface structure and chemical stability.[26,27] UDDs contain a carbon matrix with sp^3 rich carbon atoms that is responsible for good thermal conduction, but poor electron conductivity. Until now, onion-like carbons have been fabricated from UDD at very high temperatures to introduce sp^2 hybridized sites.[28] Moreover, improved metal free catalysts that can be employed for transfer hydrogenation reactions are still desired.

A main point is that a catalyst capable of performing hydrogenation without the use of metals and hydrogen gas is highly desirable.

[a] *Department of Chemistry and Chemical Sciences, Central University of Himachal Pradesh, Academic Block Shahpur, Dharamshala, Kangra (H.P.) 176215, India. E-mail: gupta_nrj@yahoo.co.in*
[b] *School of Physics and Materials Science, Shoolini University of Biotechnology and Management Sciences, Solan, 173229, India*
[c] *Department of Materials Science, University of Milano-Bicocca, Via Cozzi 55, 20125 Milano, Italy. E-mail: giovanni.diliberto@unimib.it*
[d] *Dipartimento di Chimica, Università degli Studi di Milano, Via Golgi 19, 20133 Milano, Italy. E-mail: alberto.villa@unimi.it*

† Electronic supplementary information (ESI) available. See DOI: https://doi.org/10.1039/d4qm01107d

Herein, a new catalytic method is presented to replace the use of costly and highly flammable hydrogen gas for styrene hydrogenation that shows good activity for transfer hydrogenation reaction. The three different catalysts BN-UDD-550, BN-UDD-675 and BN-UDD-800 were fabricated using precursors UDD and BN-polymeric membrane at different temperatures. The present method provides a novel material, in which a sp^2 hybridized conducting layer (derived from BN-polymeric membrane) was introduced on the surface of UDD without any exfoliation of its structure. The prepared catalysts were employed for the hydrogenation of styrene by adopting two strategies. The hydrogenation was carried out with isopropanol and also with the help of hydrogen gas, where the former is crucial to enhance safety control in the hydrogenation process.

2. Experimental

The details of chemicals and materials used along with characterization details are given in the ESI.†

2.1. Synthesis of BN-polymeric membrane

BN-polymeric membrane was manufactured using a laboratory-scale electrospinning machine. The polyaniline (PAN) powder (1.5 g) was dissolved in 20 mL of DMF at 80 °C and kept under constant stirring for 12 h until a clear polymer solution was obtained. After the preparation of the PAN solution, 0.5 g of boric acid was added under vigorous stirring for 4 hours. The PAN–boric acid solution was loaded into a 5 mL syringe with a metallic needle for electrospinning. The metallic needle of the syringe was clipped to the positive terminal of a high-voltage power supply at 15 kV at a flow rate of 1 mL h^{-1}. The other terminal was connected to the rotating drum collector (150 rpm), and the aluminium foil was fixed on the collector approximately 15 cm away from the tip of the metallic needle. The polymer solution was transformed into a nanofiber sheet on the collector and the obtained material was designated as BN-polymeric membrane (300 mg).

2.2. Fabrication of the catalyst

Ultra-dispersed diamond (UDD) (250 mg) was covered with BN polymeric membrane (250 mg). The contents were heated under an inert atmosphere (nitrogen gas) by raising the temperature at a rate of 10 °C min^{-1} to 550 °C. It was held at 550 °C for 5 min followed by cooling to room temperature under nitrogen gas. The material was taken out and labelled as BN-UDD-550 (264 mg). Other materials were prepared similarly but with the temperature raised to 675 °C and 800 °C to get BN-UDD-675 (140 mg) and BN-UDD-800 (102 mg), respectively.

2.3. Styrene hydrogenation

Styrene hydrogenation was performed in a stainless steel reactor (with a capacity of 30 mL) equipped with a gas supply system, a glass inlet, a mechanical stirrer, a heater and a thermometer. Styrene solution in 2-propanol (10 mL, 0.05 M) was added into the reactor and the desired amount of the catalyst (styrene : catalyst = 10 : 1 wt/wt) was suspended in the solution. The pressure of the hydrogen was 5 bar. The mixture was heated at 120 and 150 °C and mechanically stirred (1250 rpm) for 6 hours. At the end of the reaction, the autoclave was cooled down to room temperature, the hydrogen flow stopped and the autoclave was purged with flowing nitrogen. The hydrogen transfer reaction was performed under N_2 (5 bar). The samples were periodically collected (0.2 mL) and analysed using gas chromatography. The external standard (*n*-octanol) method was used to quantify the products and reagents.

2.4. Computational details

Spin polarized DFT calculations were performed with the VASP code[29–31] using the generalized gradient approximation, as implemented in the PBE functional.[32] The valence electrons were expanded on a set of plane waves with a kinetic energy cutoff of 400 eV, whereas the core electrons were treated with the projector augmented wave approach (PAW).[33,34] The threshold criteria for electronic and ionic loops were set to 10^{-5} eV and 10^{-2} eV $Å^{-1}$, respectively.

The sampling of the reciprocal space was adapted to provide converged results. Dispersion forces have been included according to the Grimme's D3 parametrization.[35] Single point PBE0[36,37] calculations have been performed to refine the electronic structure.[38] This is typically a reasonable choice to provide accurate results without the need for performing computationally demanding geometry optimizations with hybrid functionals.

The catalyst was modelled as a single graphene nanosheet. The catalyst was obtained upon full optimization of the unit cell and generation of a supercell. The working lattice vectors are (a = 9.870 Å, b = 9.870 Å, γ = 120°),[39,40] considering the presence of a vacuum layer of 15 Å to avoid spurious effects due to interaction between periodic replica of the system along the nonperiodic direction. We then created different nitrogen and boron-doped graphene models following experimental insights. In each case, the atomic coordinates were fully relaxed.

The Gibbs energies were evaluated by adopting the *ab initio* thermodynamic approach,[41,42] by adding to the DFT energy the contribution of zero-point energy correction and entropy terms (Table S1, ESI†). We neglected any reaction barriers different from those arising from thermochemistry to construct free energy profiles.[43,44] Zero-point energies were calculated in a harmonic fashion. Entropies of gas phase species were taken from the international tables, and the entropy of solid-state species was determined through the formalism of the partition function. The Gibbs free energy profiles were determined, assuming them to work at T = 150 °C and P = 5 atm.

3. Results and discussion

3.1. Catalytic tests

Three catalysts were prepared by thermal annealing BN polymeric membrane with ultra-dispersed diamond (UDD) at 550 °C, 675 °C and 800 °C. The covering of a polymeric membrane on the surface of UDD during the annealing process ensures that a graphitic layer is formed on its surface. We initially reported the activity of BN-UDD-550, BN-UDD-675 and BN-UDD-800, in the

hydrogenation reaction of styrene into ethylbenzene. Afterwards, to understand the influence of material chemistry on the catalyst properties, a detailed characterization of the surface properties was reported.

Table 1 Catalytic results for styrene hydrogenation under a hydrogen or nitrogen atmosphere

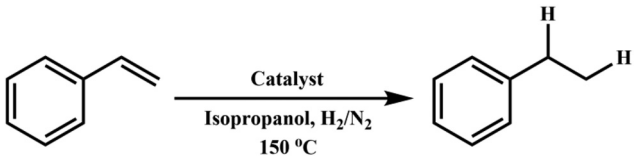

S. no.	Catalyst	Reaction environment	Conversion (%) after 6 h	Selectivity (%)
1	None	H_2 or N_2	—	—
2	BN-UDD-550	H_2	33.0	99
		N_2	18.2	99
3	BN-UDD-675	H_2	65.3	99
		N_2	30.2	99
4	BN-UDD-800	H_2	28.4	99
		N_2	13.4	99

Reaction conditions: 10 mL styrene solution in isopropanol (0.05 M) and catalyst (10 mg) were stirred for 6 hours under H_2 or N_2 (5 bar) at 150 °C.

The reaction was performed in a stainless steel autoclave at 150 °C in the presence of hydrogen (5 bar H_2) using isopropanol as the solvent. The catalyst amount and the stirring rate and reaction temperature were chosen to perform the reaction under a kinetic regime and to obtain a good activity without influencing the stability of the catalysts.[16] The product formation was monitored by gas chromatography sampling the solution every 2 hours. The reaction was also performed in the absence of catalyst and no conversion was observed. Comparing the activity after 6 h of reaction (Table 1), we observed that the most active catalyst was BN-UDD-675 with a conversion of 65.5%, followed by BN-UDD-550 (33.0%) and BN-UDD-800 (28.4%). Plotting the conversion *versus* time (Fig. 1) it is possible to observe that the reaction proceeds without evident deactivation phenomena regardless of the catalytic material tested. All the catalysts showed almost total selectivity to ethylbenzene (>99%). The catalysts were also tested in the catalytic transfer hydrogenation of styrene in the absence of H_2 using 2-propanol as the H-donor (Table 1). When H_2 is replaced by N_2, a lower conversion is observed. However, the catalysts showed the same trend in the activity, BN-UDD-675 (30.2%) > BN-UDD-550 (18.2%) > BN-UDD-800 (13.4%).

The effect of the temperature was evaluated by testing the catalysts at 120–150 °C in the presence of H_2 or N_2 (Fig. 1) to

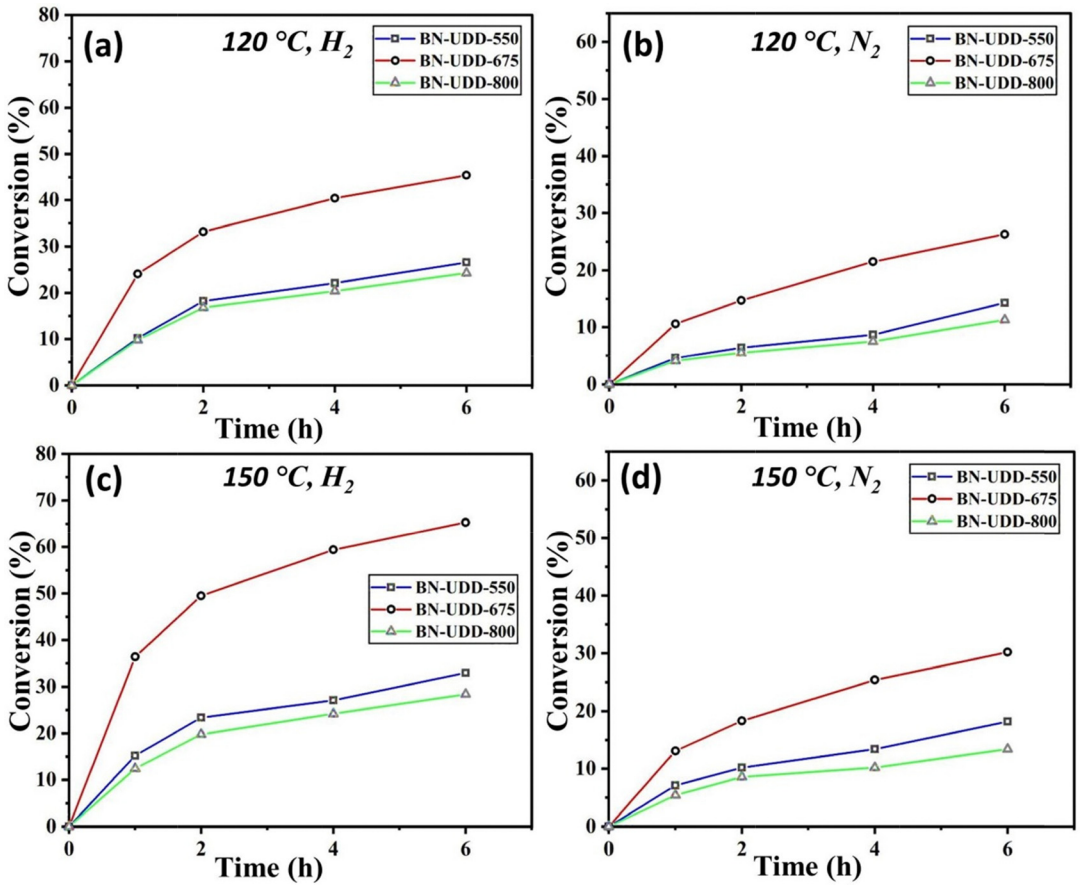

Fig. 1 Conversion *vs.* time graphs of different catalysts at (a) 120 °C under H_2 gas, (b) 120 °C under N_2 gas, (c) 150 °C under H_2 gas, and (d) 150 °C under N_2 gas.

check for the presence of trends. As expected, an increase of the reaction temperature is beneficial for the activity, maintaining the selectivity >99% (Fig. S1, ESI†). There is no effect on the selectivity that was found >99% for all the temperatures considered. The turnover frequency (TOF) of all the catalysts for styrene hydrogenation was calculated and reported in Table S2 (ESI†). The catalysts BN-UDD-550, BN-UDD-675 and BN-UDD-800 show the TOF of 1.76, 2.71 and 1.68 h^{-1} respectively, in the presence of hydrogen gas. A comparison of the TOF of the prepared catalysts with metal-free catalysts is presented in Table S2 (ESI†). The TOF of the synthesized catalysts is comparable to that of other metal-free catalysts used in similar reactions. The stability of the most active catalyst, BN-UDD-675, was investigated at 150 °C in the presence of H_2, by recycling the catalyst for 8 runs, without any pretreatment between each cycle (Fig. S2, ESI†). The catalyst showed a slight decrease in the conversion between the first and the second run, becoming stable for the successive cycles.

The nature of the hydrogenation catalysts is further revealed thoroughly by characterizing BN-UDD-675. Initially the crystallinity, structural configuration and phase formation of the catalyst were observed by X-ray diffraction (XRD) analysis. The XRD pattern (Fig. 2a) indicates the broader and high intensity peaks centered at 2θ values of 14.8°, 25.5°, 28°, 42.8° and 57.6°. A minor peak at 42.8° is characteristic of the (111) *hkl* plane reflection[45] in the lattice of UDD. However, there is a distinct difference in the peak intensity, which indicates a change in their nature. The broader peak observed at 25.5° corresponds to an experimental *d*-spacing of 3.48 Å, indicating the existence of graphite-like carbon ($d_{(002)}$, JCPDS: 41-1487),[46] which is most likely due to the graphitization of the BN-polymeric membrane at high temperature.[47] Moreover, two peaks are observed at 14.8° and 28° (intense peak) corresponding to crystallographic planes denoted as (100) and (002), respectively, corresponding to graphitic carbon nitride (g-C_3N_4).[48] The peaks at 28° (002) combined with the one at 57.6° (004) correspond to the hexagonal boron nitride (h-BN).[49,50] These peaks signify the successful incorporation of B into the graphitic sheets along with the presence of UDD in the prepared catalyst. The presence of boron nitride also indicates that key active sites bearing a –B═N– moiety are also present in it. The high intensity peak at 28.07° strongly implies the crystalline nature of the synthesized carbon structure. The structural parameters, micro-crystallite width (L_a) and stack height of the micro crystallites (L_c) are calculated to be 2.17 and 1.05 nm, respectively.

The morphology of the BN-UDD-675 catalyst was investigated through FESEM (Fig. 2) and HRTEM analysis (Fig. 3). The FESEM images (Fig. 2b and c) illustrate the irregular oval-shaped structures forming the sheets that are stacked above one another. It is a tapered oval stack, where the constituting units are cross-linked with pores in between them with definite grain boundaries. The random distribution of grains also indicates that the BN-polymeric membrane can function as a good precursor to generate large surface area and pore structures on the UDD surface. The histogram (Fig. 2d) shows that the average size of these oval structures is 121 nm.

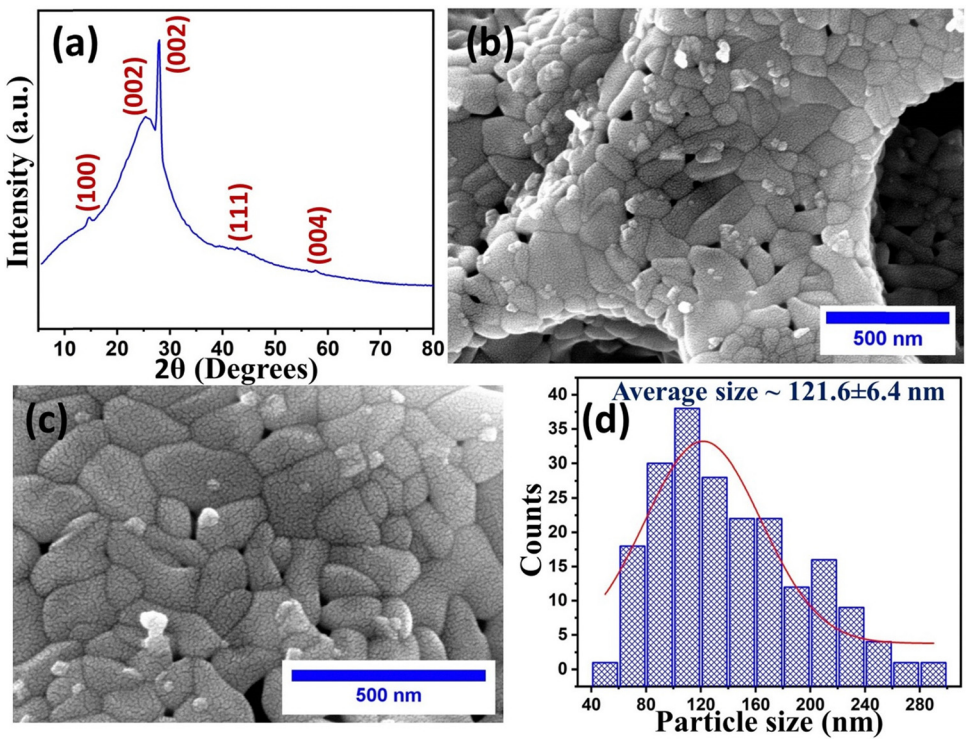

Fig. 2 (a) XRD spectrum of the BN-UDD-675 catalyst, showing a broader peak at 25.5° indicating the existence of graphite-like carbon. (b) and (c) FESEM images of the BN-UDD-675 catalyst, showing the irregular oval-shaped structures and (d) particle size histogram (Fig. 2b was used to calculate the particle size).

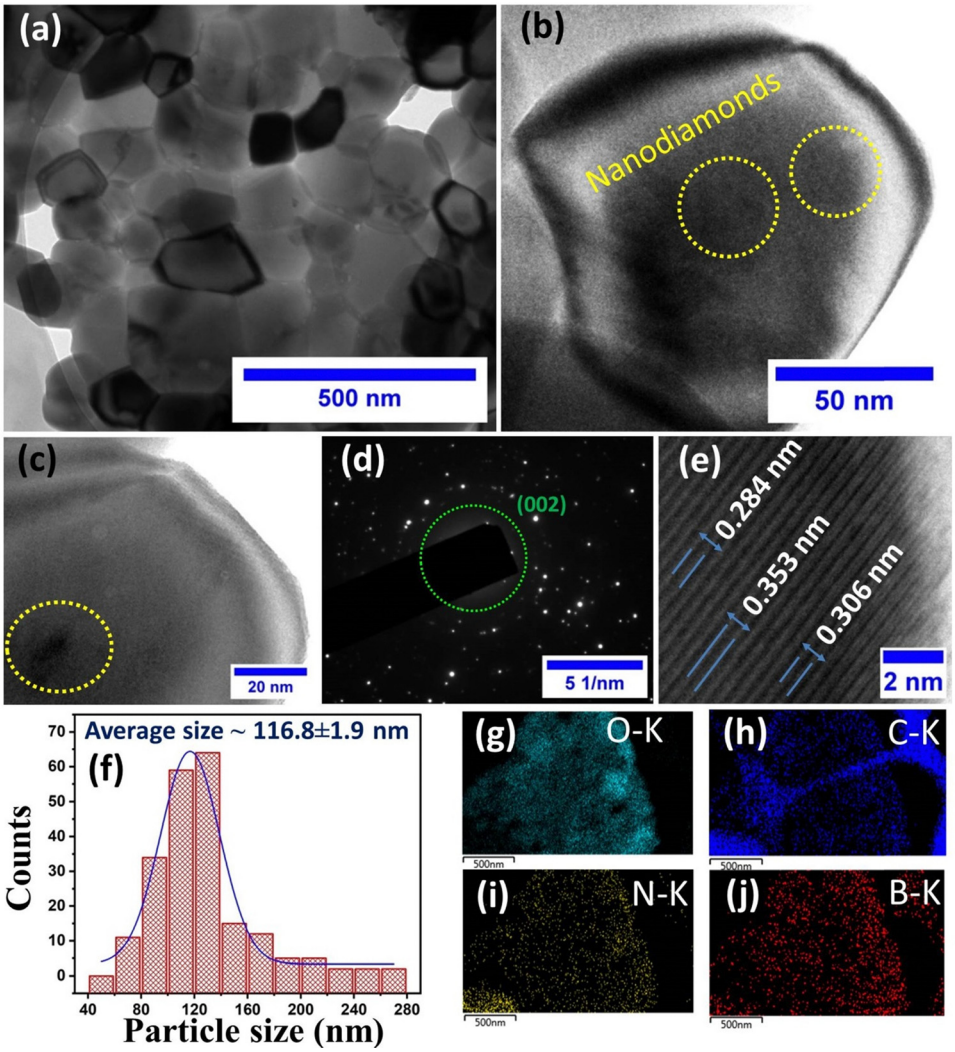

Fig. 3 (a) HRTEM image of the BN-UDD-675 catalyst; (b) and (c) individual constituents of the tapered oval stack structure showing the presence of small rounded particles in between them that are highlighted by the yellow color; (d) SAED pattern, (e) interplanar spacing, (f) particle size histogram (particle size was calculated using Fig. 3a), and (g)–(j) elemental mapping images of the BN-UDD-675 catalyst.

The surface structures observed in these cases are completely different from the ingredient UDD used in catalyst preparation. Therefore, HRTEM analysis was further carried out to provide more insight into the structure (Fig. 3). These images also show oval structures with well-defined dark boundaries connected. Specifically, these are polygonal structures linked to each other that are found to encapsulate small spherical structures in between them (Fig. 3b). The approximate particle size of these spherical structures present inside is 15 nm, which is most probably due to the UDD used as a precursor. These images confirm that the UDD is covered with many layers of graphitic sheets generated by thermal annealing of the BN-polymeric membrane. The linkage between these polygonal structures might be possible due to π–π stacking between the graphitic layers. Additionally, Fig. 3e shows the well crystalline interplanar spacing in the regular arrangement of the atoms. The narrow ring with a 3.63 Å *d*-spacing and (002) diffraction facet in the selected area electron diffraction (SAED) pattern (Fig. 3d) suggests that the material has successfully attained a graphite-like crystalline structure.[51] The element mapping (Fig. 3g–j and Fig. S2, S3, ESI†) reveals the presence of nitrogen, boron, carbon and oxygen within the material confirming that both nitrogen and boron have been incorporated into the catalyst. The average particle size determined from the HRTEM images is approximately 116 nm, which is almost the same as those shown by the FESEM images.

The surface nature and chemical composition of all three catalysts were probed through XPS analysis (Fig. 4) to understand the difference in their activity. The survey spectra (Fig. 4a) of BN-UDD-675, which has performed best in these catalytic tests, shows the presence of carbon, nitrogen, oxygen and boron (Table 2). The atomic percentage composition of the elements in the BN-UDD-675 catalyst, as determined by XPS analysis, reveals 58.1% C 1s, 23% O 1s, 8.6% N 1s, and 10.3% B 1s.

The boron and nitrogen spectra were further deconvoluted to identify the BN bond and other surface nitrogen-containing functional groups. The boron spectrum was deconvoluted into two

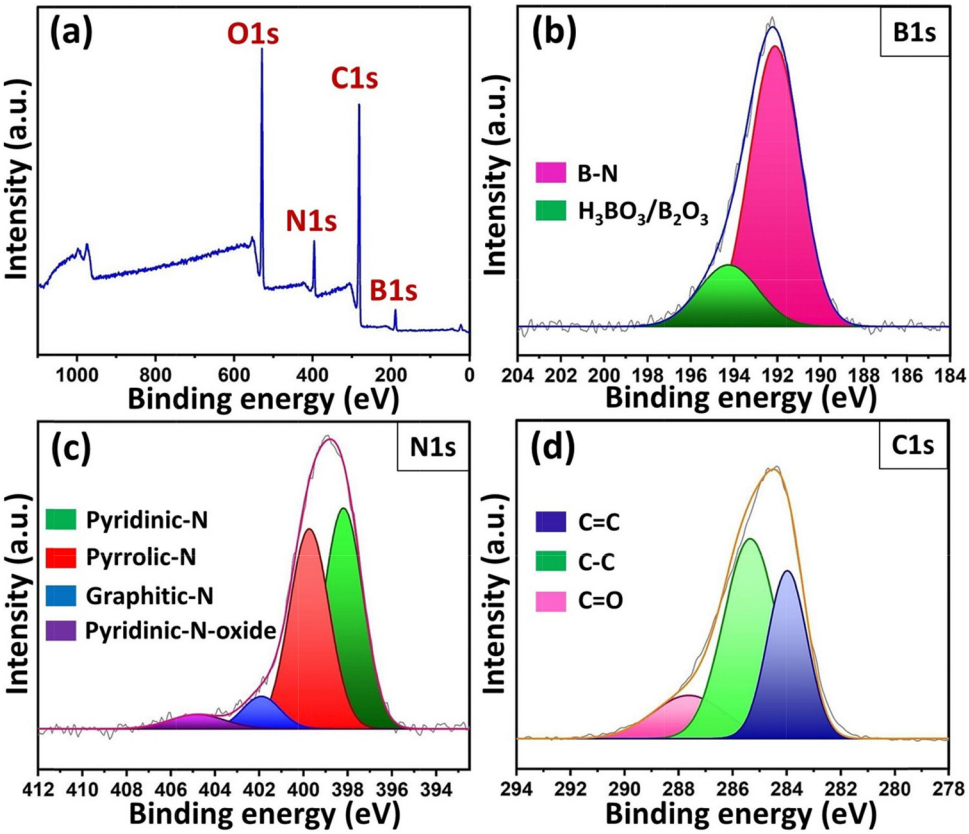

Fig. 4 (a) XPS survey spectrum of BN-UDD-675; deconvoluted high-resolution XPS spectra of (b) B 1s, (c) N 1s and (d) C 1s regions for BN-UDD-675. The peak at 192.1 eV in the B 1s spectrum can be assigned to the B–N bond indicating a direct interaction between the two dopant atoms.

Table 2 Comparison of the XPS results of different catalysts

Catalyst		Pyridinic-N	Pyrrolic-N	Graphitic-N	Pyridinic-N-oxide	B–N	H_3BO_3/B_2O_3	O–C–N–B (%)
BN-UDD-550	BE (eV)	398.2	399.7	401.8	404.8	191.9	194.6	19–67.5–3.9–9.6
	%	*46.1*	*31.5*	*16.3*	*6.1*	*55*	*45*	
BN-UDD-675	BE (eV)	398.2	399.7	401.9	404.8	192.1	194.3	23–58.1–8.6–10.3
	%	*46.6*	*42.6*	*6.6*	*4.2*	*79.5*	*20.5*	
BN-UDD-800	BE (eV)	398.3	399.8	401.7	404.6	191.8	194.2	20.8–66.1–3.8–9.3
	%	*52.7*	*26.9*	*13.7*	*6.7*	*48.3*	*51.7*	

peaks at 192.1 eV and 194.3 eV. The peak at 192.1 eV is assigned to the B–N bond[52] incorporated into the carbon matrix (Fig. 4b), indicating a direct interaction between the two dopant atoms. Another peak at 194.3 eV is assigned to oxides of boron[16] (B_2O_3 or H_3BO_3) and its presence on the catalyst surface may be due to the oxidation of elemental boron. The N 1s deconvoluted spectrum (Fig. 4c) exhibits four peaks at 398.2 eV, 399.7 eV, 401.9 eV and 404.8 eV due to the presence of pyridinic-N, pyrrolic-N, graphitic-N and pyridinic-N-oxide, respectively,[53] with a main predominance of pyridinic-N and pyrrolic-N, Fig. 4c. Finally, the carbon spectrum was deconvoluted (Fig. 4d) to see the nature of the carbon atoms, which was found to be rich in sp^2 C content (peak at 284 eV).[54] The peak at 285.3 eV corresponds to the presence of sp^3 C–C bonds,[55] while the peak at 287.6 eV indicates the presence of C═O bonds.[56] This shows that the carbon matrix is rich in sp^2 hybridised carbon atoms containing pyridinic C═N bonds, and there is the presence of B═N bonds as well.

3.2. Identification of active sites

The surface functional groups of all three catalysts BN-UDD-550, BN-UDD-675 and BN-UDD-800 were identified through XPS spectra (Fig. S6, ESI†) and carbon, nitrogen, oxygen and boron were present on their surface (Fig. S4 and S5, ESI†). The BN-UDD-675 exhibits a higher percentage composition of nitrogen (8.6%) and boron (10.3%) as compared to the other catalysts. The B 1s and N 1s spectra of all three catalysts were deconvoluted into respective nitrogen and boron-containing functional groups and their percentage composition is given in Table 2. The catalyst BN-UDD-675 displays a high percentage composition of B–N bonds (79.5%) in comparison to the other two catalysts (Fig. S6, ESI†).

The active site was identified by plotting the catalytic conversion against the percentage composition of surface functional groups. All the nitrogen containing functional groups such as pyrrolic-N, pyridinic-N and graphitic-N along with the BN bond were chosen for the correlation. The conversion does not show a linear relationship with the overall percentage of nitrogen (Fig. S7, ESI†). Contrary to this, a linear relationship is observed between overall boron percentages with conversion. The combination of these observations may suggest that boron has a direct implication in the catalyst process and the different nitrogen containing groups are probably not associated with the hydrogenation process. The nature of the boron functionality was further confirmed by plotting the B–N bond with the conversion that displays a linear correlation confirming its role in the catalytic process. Finally, the pyrrolic-N group among the nitrogen-containing functional groups also displays a linear relationship with the conversion, confirming that this might also be involved in this conversion. Therefore, it is confirmed that a B–N bond most probably in pyrrolic form is involved in the metal-free hydrogenation of styrene.

3.3. DFT analysis

Our evidence indicates that B═N bonds are involved in this reaction The XAS analysis shows that pyrrolic-N and pyridinic-N are predominant followed by a small amount of graphitic-N. We took insight from the experimental evidence and considered six different models all having a B–N bond in the structure (Fig. 5). The first one is a graphitic N configuration with a neighboring B atom and labeled as N–B (Fig. 5a). Three different pyridinic configurations were considered; where the first case involves three substitutional N atoms (3N-B) surrounding a carbon vacancy and one N directly bonded to B (Fig. 5b). The remaining two cases are based on pyridinic-N (4N-B and 4N-B_2). These three structures differ in the positioning of the boron atom (Fig. 5b–d). Finally, two pyrrolic structures (N-Bpyr_1 and N-Bpyr_2) are also considered (Fig. 5e and f), where the first structure involved a direct B–N bond in the five membered ring. Fig. S8 (ESI†) shows that a fraction of surface B atoms can be saturated by O species, forming borate residues, explaining the possible presence of oxygen atoms on the surface. These saturated species are, however, not able to bind isopropanol, and therefore can be considered not active during the reaction.

The reaction was modelled by considering the oxidation of isopropanol to acetone, where hydrogen species are chemically adsorbed to the catalyst, eqn (1).

$$CH_3CHOHCH_3 \rightarrow CH_3COCH_3 + 2H^* \quad (1)$$

Then, if the catalyst can adsorb styrene the reaction can proceed forming ethylbenzene (eqn (2)), or the system can release molecular hydrogen (eqn (3)). The reaction scheme is sketched in Fig. 6.

$$CH_3CHOHCH_3 + PhCHCH_2 \rightarrow CH_3COCH_3 + PhCH_2CH_3 \quad (2)$$

$$CH_3CHOHCH_3 \rightarrow CH_3COCH_3 + H_2 \quad (3)$$

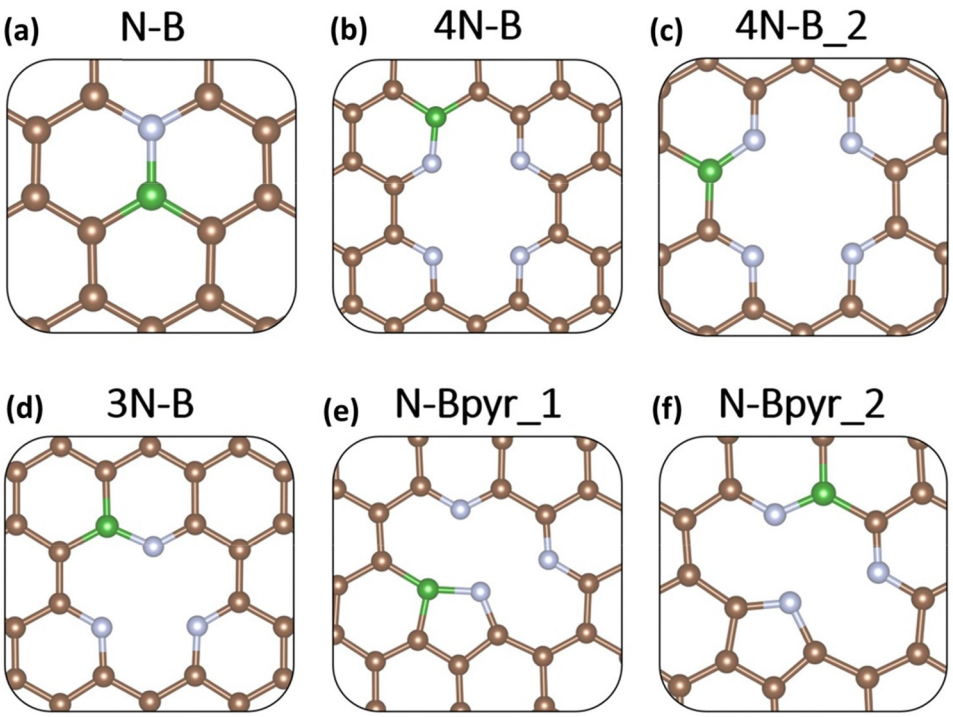

Fig. 5 Structures of different catalytic sites investigated with heteroatom B and N doped in the carbon matrix. The brown, grey and green balls correspond to C, N and B atoms, respectively. In particular, six models are reported: graphitic N configuration with a neighboring B atom (a); three different pyridinic configurations labelled 4N-B (b), 4N-B_2 (c) and 3N-B (d); and finally, two cases based on pyridinic-N (e and f).

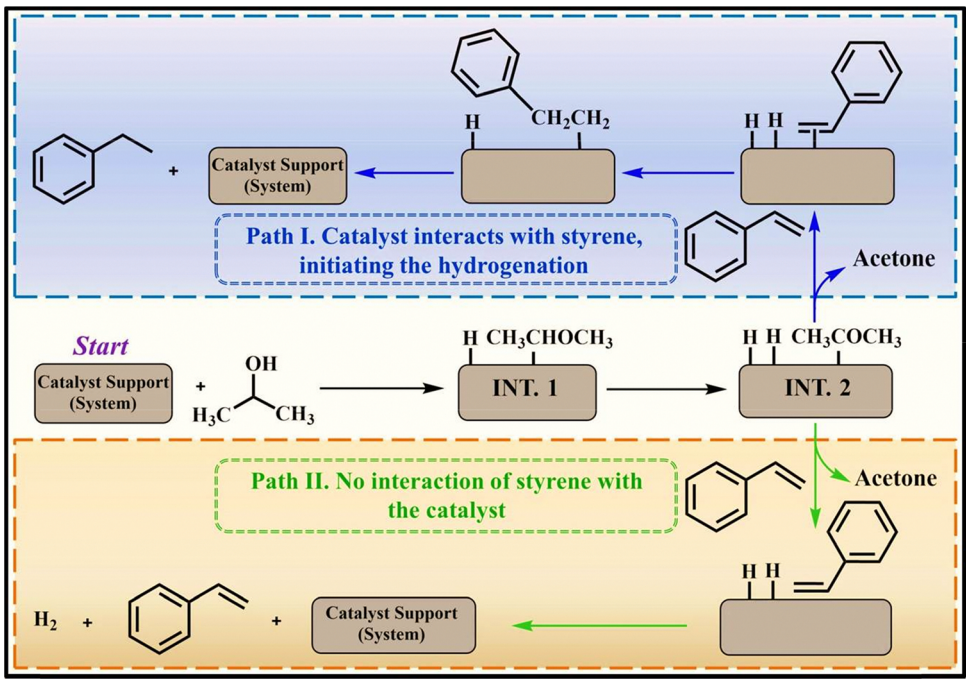

Fig. 6 Possible reaction pathways for the transfer hydrogenation involving isopropanol.

The analysis of the Gibbs free energy profiles of the graphitic catalyst (Fig. S9, ESI†) indicates that the system is not able to catalyze the reaction, as the intermediates are very unstable. Conversely, in the pyridinic-N cases, Fig. S10–S12 (ESI†), very stable adducts are always formed with barriers reaching up to 1.9 eV for desorption of the products (acetone and H_2). Also, styrene does not bind the catalyst, and therefore the reaction would proceed by releasing molecular hydrogen and acetone.

More interesting is the case of the pyrrolic-N catalyst, as in this case, the activation of isopropanol leads to three possible adsorption configurations that are nearly isoenergetic, as shown in Fig. 7a. More specifically, the hydrogen atom can bind a N-species or a carbon atom next to the boron dopant. Moving to the second reaction step, two hydrogen adducts adsorbed on N-species lead to a structure which is very stable and poisons the catalyst, as the system is not able to bind styrene, leading to the formation of acetone and molecular H_2, with a very large barrier to release the products (Fig. 7b). In the other two cases, where one hydrogen atom is bound to a carbon and the second atom binds a nitrogen atom, the reaction can proceed *via* the release of acetone and the adsorption of hydrogen species (H*) that can interact with styrene when it is adsorbed. The two situations reported in Fig. 7c and d differ by the relative positioning of the H* species, where the two H* adsorbed to the catalyst are far apart (Fig. 7c), or are adsorbed to the nearest neighboring atoms (Fig. 7d). In both cases the maximum reaction barrier is 0.98 eV, which is compatible with other organic reactions conducted on carbon-based catalysts.[57,58]

The remaining pyrrolic catalyst is less interesting, as the catalyst is too reactive leading to very stable reaction intermediates, without adsorbing styrene (Fig. S13, ESI†). Among the models considered, the only phase that can catalyze the reduction of styrene to ethylbenzene is made by the pyrrolic-N model where boron occupies a five-membered ring. Table S3 (ESI†) summarizes the reaction barriers for the different catalysts. Only N_Bpyr1 is able to promote the reaction towards ethylbenzene. The remaining systems are not able to bind styrene and should stop the reaction to acetone and H_2.

Solvation is an important ingredient in computational catalysis.[59,60] This can be achieved by explicitly simulating the material/solvent interface, with a sufficiently thick model for the solvent, to reproduce a bulk-like behavior.[61,62] This is typically computationally hard to address, especially when trying to include dynamics effects, due to the need of with *ab initio* molecular dynamics. An alternative way is implicit solvation.[63,64] Here, the action of the solvent is replaced by a continuum dielectric. We refined our results by recalculating the reaction profiles with the lowest barriers. The effect of the solvent is rather small as can be evinced by looking at Fig. S14 (ESI†), and the maximum barrier, which changes by 0.02 eV only.

Therefore, based on these calculations, the nature of the defects having B–N species determines the reactivity. The reaction starts from the adsorption of isopropanol and the abstraction of hydrogen to form the isopropoxide ion, which gets stabilized by the B atom. There are two possible reaction routes. In one case, the catalyst is able to bind styrene, promoting its reduction to ethylbenzene with the release of acetone. Alternatively, if styrene adsorption is not favorable, one more H atom is abstracted from isopropoxide, released from the surface acetone and H_2. Among all catalytic models, the pyrrolic structure

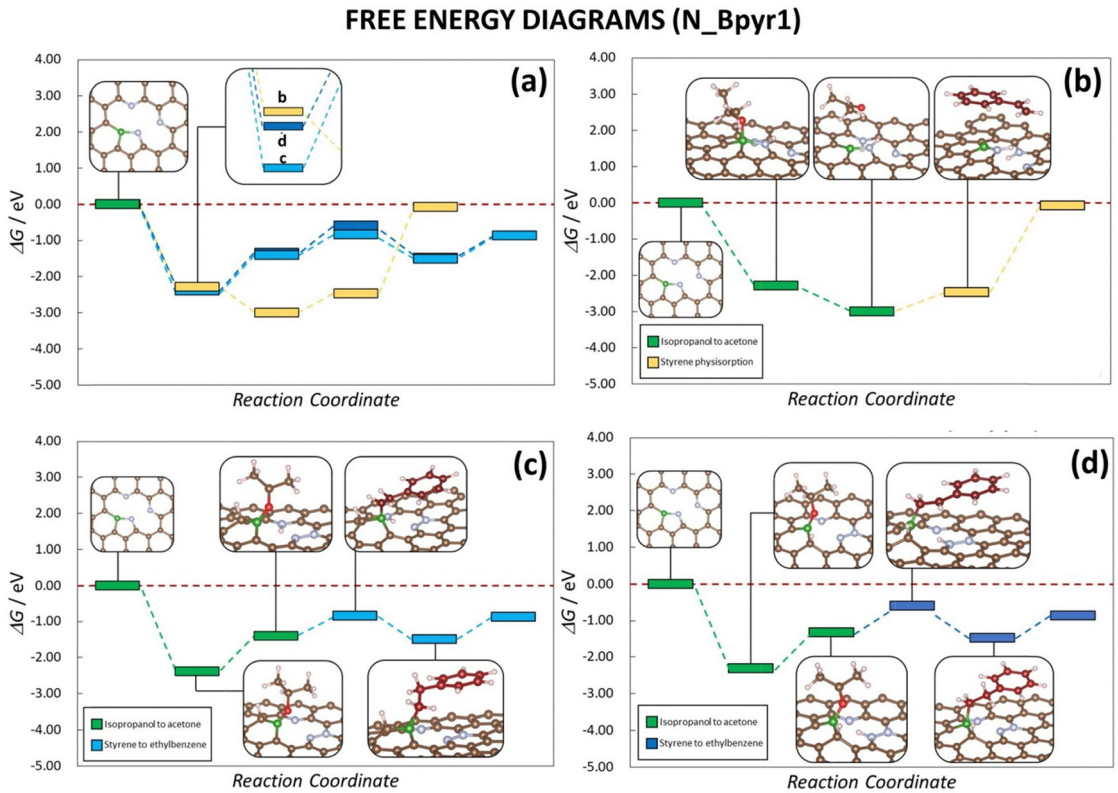

Fig. 7 (a) Free energy profile of the reaction conducted on a pyrrolic N site showing three nearly isoenergetic possible adsorption configurations, and (b)–(d) individual free energy profiles for each of the three configurations. Brown, grey, green, red and pinkish white balls correspond to C, N, B, O and H atoms, respectively.

involving a direct B–N bond in the five membered ring can promote styrene hydrogenation to ethylbenzene.

4. Conclusions

Metal-free catalysts were synthesized utilizing UDD and BN-polymeric membrane and successfully applied for the direct hydrogenation of styrene to ethyl benzene. The incorporation of B and N species in the matrix was confirmed by combining XRD, EDS and XPS analysis. We provide evidence of direct B–N interactions. Electron microscopy revealed the presence of meso-crystal porous structures formed by the stacking of polygonal structures. The catalysts were successfully used for the hydrogenation of styrene both in the presence and absence of hydrogen gas. Importantly, the catalysts were active in the absence of hydrogen gas using isopropanol. Quantum chemical simulations provided an atomistic description of the catalytic process, where the reaction is likely to occur on pyrrolic-N defects where B occupies a five-membered ring. This finding provides new insights into understanding the role of B and N functionalities in hydrogenation reaction when integrated into a carbon matrix and a promising direction for the application of carbon materials. In particular, it might be possible to enhance the activity by tuning the B–N/N ratio. Future work will be dedicated to the characterization of the active phase by combining XPS and other techniques like electron energy loss spectroscopy (EELS), to determine the nature of the light elements. Moreover, the impact of different hydrogen donors, such as methanol and formic acid, on the final reactivity of the metal free carbons in hydrogenation reactions will be considered.

Author contributions

NG conceptualized the work and designed the catalysts for this reaction. AS synthesized the materials with the assistance of MS and SK (who performed the electro-spinning). AV and IB performed all the catalytic tests. GDL and EI performed the DFT analysis. The manuscript was collectively written by AS and NG, and was internally revised by AV and GDL.

Data availability

The data reported in this article can be found in the literature cited and can be obtained from the authors upon reasonable request.

Conflicts of interest

The authors declare that they have no known competing financial interests or personal relationships that could have appeared to influence the work reported in this article.

Acknowledgements

Access to the CINECA supercomputing resources was granted *via* ISCRAB. We also thank the COST Action 18234 supported by COST (European Cooperation in Science and Technology).

References

1 Z. Niu, W. Zhang, P. C. Lan, B. Aguila and S. Ma, Promoting Frustrated Lewis Pairs for Heterogeneous Chemoselective Hydrogenation via the Tailored Pore Environment within Metal–Organic Frameworks, *Angew. Chem., Int. Ed.*, 2019, **58**, 7420–7424.

2 J. Gao, R. Ma, L. Feng, Y. Liu, R. Jackstell, R. V. Jagadeesh and M. Beller, Ambient Hydrogenation and Deuteration of Alkenes Using a Nanostructured Ni-Core–Shell Catalyst, *Angew. Chem., Int. Ed.*, 2021, **133**, 18739–18746.

3 W. Ludwig, A. Savara, K. H. Dostert and S. Schauermann, Olefin hydrogenation on Pd model supported catalysts: new mechanistic insights, *J. Catal.*, 2011, **284**, 148–156.

4 M. Cao, K. Miyabayashi, Z. Shen, K. Ebitani and M. Miyake, Olefin hydrogenation catalysis of platinum nanocrystals with different shapes, *J. Nanopart. Res.*, 2011, **13**, 5147–5156.

5 T. Wang, C. Pranckevicius, C. L. Lund, M. J. Sgro and D. W. Stephan, Ruthenium Carbene–Diether Ligand Complexes: Catalysts for Hydrogenation of Olefins, *Organometallics*, 2013, **32**, 2168–2177.

6 E. Alberico, W. Baumann, J. G. De Vries, H. J. Drexler, S. Gladiali, D. Heller, H. J. W. Henderickx and L. Lefort, Unravelling the reaction path of rhodium-monophos-catalysed olefin hydrogenation, *Chem. – Eur. J.*, 2011, **17**, 12683–12695.

7 S. Ghosh and B. R. Jagirdar, Synthesis of mesoporous iridium nanosponge: a highly active, thermally stable and efficient olefin hydrogenation catalyst, *Dalton Trans.*, 2017, **46**, 11431–11439.

8 D. J. Nash, D. T. Restrepo, N. S. Parra, K. E. Giesler, R. A. Penabade, M. Aminpour, D. Le, Z. Li, O. K. Farha, J. K. Harper, T. S. Rahman and R. G. Blair, Heterogeneous metal-free hydrogenation over defect-laden hexagonal boron nitride, *ACS Omega*, 2016, **1**, 1343–1354.

9 Y. Qin, J. Lu, Z. Zou, H. Hong, Y. Li, Y. Li, L. Chen, J. Hu and Y. Huang, Metal-free chemoselective hydrogenation of unsaturated carbon–carbon bonds: via cathodic reduction, *Org. Chem. Front.*, 2020, **7**, 1817–1822.

10 A. Willms, H. Schumacher, T. Tabassum, L. Qi, S. L. Scott, P. J. C. Hausoul and M. Rose, Solid Molecular Frustrated Lewis Pairs in a Polyamine Organic Framework for the Catalytic Metal-free Hydrogenation of Alkenes, *ChemCatChem*, 2018, **10**, 1835–1843.

11 Y. Imada, T. Kitagawa, T. Ohno, H. Iida and T. Naota, Neutral flavins: green and robust organocatalysts for aerobic hydrogenation of olefins, *Org. Lett.*, 2010, **12**, 32–35.

12 A. M. Faísca Phillips and A. J. L. Pombeiro, Recent advances in organocatalytic enantioselective transfer hydrogenation, *Org. Biomol. Chem.*, 2017, **15**, 2307–2340.

13 P. Chen, L. M. Chew, A. Kostka, K. Xie, M. Muhler and W. Xia, Purified oxygen- and nitrogen-modified multi-walled carbon nanotubes as metal-free catalysts for selective olefin hydrogenation, *J. Energy Chem.*, 2013, **22**, 312–320.

14 A. Primo, F. Neatu, M. Florea, V. Parvulescu and H. Garcia, Graphenes in the absence of metals as carbocatalysts for selective acetylene hydrogenation and alkene hydrogenation, *Nat. Commun.*, 2014, **5**, 1–9.

15 A. Dhakshinamoorthy, J. He, A. Franconetti, A. M. Asiri, A. Primo and H. Garcia, Defective graphene as a metal-free catalyst for chemoselective olefin hydrogenation by hydrazine, *Catal. Sci. Technol.*, 2018, **8**, 1589–1598.

16 A. Dogra, I. Barlocco, A. Singh, F. Somodi, A. Villa and N. Gupta, Metal free alkene hydrogenation by B-doped graphitic carbon nitride, *Catal. Sci. Technol.*, 2020, **10**, 3024–3028.

17 J. C. Espinosa, S. Navalon, M. Alvaro, A. Dhakshinamoorthy and H. Garcia, Reduction of C═C Double Bonds by Hydrazine Using Active Carbons as Metal-Free Catalysts, *ACS Sustainable Chem. Eng.*, 2018, **6**, 5607–5614.

18 P. Chen, L. M. Chew, A. Kostka, M. Muhler and W. Xia, The structural and electronic promoting effect of nitrogen-doped carbon nanotubes on supported Pd nanoparticles for selective olefin hydrogenation, *Catal. Sci. Technol.*, 2013, **3**, 1964–1971.

19 E. Sikora, A. Kiss, Z. H. Göndör, P. Pekker, F. Kristály, M. Szőri, A. Rágyanszki, B. Viskolcz, B. Fiser and L. Vanyorek, Fine-tuning the catalytic activity by applying nitrogen-doped carbon nanotubes as catalyst supports for the hydrogenation of olefins, Reaction Kinetics, *Mech. Catal.*, 2020, **129**, 95–106.

20 Y. Zhang, J. Guo, P. VanNatta, Y. Jiang, J. Phipps, R. Roknuzzaman, H. Rabaâ, K. Tan, T. AlShahrani and S. Ma, Metal-Free Heterogeneous Asymmetric Hydrogenation of Olefins Promoted by Chiral Frustrated Lewis Pair Framework, *J. Am. Chem. Soc.*, 2024, **146**, 979–987.

21 D. W. Stephan and G. Erker, Frustrated Lewis pair chemistry: development and perspectives, *Angew. Chem., Int. Ed.*, 2015, **54**, 6400–6441.

22 D. J. Scott, M. J. Fuchter and A. E. Ashley, Designing effective 'frustrated Lewis pair' hydrogenation catalysts, *Chem. Soc. Rev.*, 2017, **46**, 5689–5700.

23 N. Li and W. X. Zhang, Frustrated Lewis Pairs: Discovery and Overviews in Catalysis, *Chin. J. Chem.*, 2020, **38**, 1360–1370.

24 D. Wang and D. Astruc, The Golden Age of Transfer Hydrogenation, *Chem. Rev.*, 2015, **115**, 6621–6686.

25 Y. Ding, X. Huang, X. Yi, Y. Qiao, X. Sun, A. Zheng and D. S. Su, A Heterogeneous Metal-Free Catalyst for Hydrogenation: Lewis Acid–Base Pairs Integrated into a Carbon Lattice, *Angew. Chem., Int. Ed.*, 2018, **57**, 13800–13804.

26 S. Kumar, M. Nehra, D. Kedia, N. Dilbaghi, K. Tankeshwar and K. H. Kim, Nanodiamonds: emerging face of future nanotechnology, *Carbon*, 2019, **143**, 678–699.

27 N. Gupta, Q. Wang, G. Wen and D. Su, *Nanodiamonds for catalytic reactions*, Elsevier Inc., 6th edn, 2017.

28 Y. Lin, Y. Zhu, B. Zhang, Y. A. Kim, M. Endo and D. S. Su, Boron-doped onion-like carbon with enriched substitutional boron: the relationship between electronic properties and catalytic performance, *J. Mater. Chem. A*, 2015, **3**, 21805–21814.

29 G. Kresse and J. Hafner, Ab initio molecular dynamics for liquid metals, *Phys. Rev. B: Condens. Matter Mater. Phys.*, 1993, **47**, 558–561.

30 G. Kresse and J. Furthmüller, Efficiency of ab initio total energy calculations for metals and semiconductors using a plane-wave basis set, *Comput. Mater. Sci.*, 1996, **6**, 15–50.

31 G. Kresse and J. Hafner, Ab initio molecular-dynamics simulation of the liquid–metalamorphous–semiconductor transition in germanium, *Phys. Rev. B: Condens. Matter Mater. Phys.*, 1994, **49**, 14251–14269.

32 J. P. Perdew, K. Burke and M. Ernzerhof, Generalized Gradient Approximation Made Simple, *Phys. Rev. Lett.*, 1996, **77**, 3865–3868.

33 P. E. Blöchl, Projector augmented-wave method, *Phys. Rev. B: Condens. Matter Mater. Phys.*, 1994, **50**, 17953–17979.

34 D. Joubert, From ultrasoft pseudopotentials to the projector augmented-wave method, *Phys. Rev. B: Condens. Matter Mater. Phys.*, 1999, **59**, 1758–1775.

35 S. Grimme, J. Antony, S. Ehrlich and H. Krieg, A consistent and accurate ab initio parametrization of density functional dispersion correction (DFT-D) for the 94 elements H-Pu, *J. Chem. Phys.*, 2010, **132**(15), 154104.

36 C. Adamo and V. Barone, Toward reliable density functional methods without adjustable parameters: the PBE0 model, *J. Chem. Phys.*, 1999, **110**, 6158–6170.

37 J. P. Perdew, M. Ernzerhof and K. Burke, Rationale for mixing exact exchange with density functional approximations, *J. Chem. Phys.*, 1996, **105**, 9982–9985.

38 I. Barlocco, L. A. Cipriano, G. Di Liberto and G. Pacchioni, Modeling Hydrogen and Oxygen Evolution Reactions on Single Atom Catalysts with Density Functional Theory: Role of the Functional, *Adv. Theory Simul.*, 2023, **6**, 2200513.

39 I. Barlocco, G. Di Liberto and G. Pacchioni, New scaling relationships for the oxygen evolution reaction on single atom catalysts, *Catal. Today*, 2024, **427**, 114409.

40 G. Di Liberto, L. Giordano and G. Pacchioni, Predicting the Stability of Single-Atom Catalysts in Electrochemical Reactions, *ACS Catal.*, 2024, **14**, 45–55.

41 J. K. Nørskov, T. Bligaard, A. Logadottir, J. R. Kitchin, J. G. Chen, S. Pandelov and U. Stimming, Trends in the Exchange Current for Hydrogen Evolution, *J. Electrochem. Soc.*, 2005, **152**, J23.

42 J. K. Nørskov, T. Bligaard, J. Rossmeisl and C. H. Christensen, Towards the computational design of solid catalysts, *Nat. Chem.*, 2009, **1**, 37–46.

43 J. K. Nørskov, T. Bligaard, A. Logadottir, J. R. Kitchin, J. G. Chen, S. Pandelov and U. Stimming, Trends in the Exchange Current for Hydrogen Evolution, *J. Electrochem. Soc.*, 2005, **152**, J23.

44 J. K. Nørskov, T. Bligaard, J. Rossmeisl and C. H. Christensen, Towards the computational design of solid catalysts, *Nat. Chem.*, 2009, **1**, 37–46.

45 V. Kuzmin, K. Safiullin, G. Dolgorukov, A. Stanislavovas, E. Alakshin, T. Safin, B. Yavkin, S. Orlinskii, A. Kiiamov, M. Presnyakov, A. Klochkov and M. Tagirov, Angstrom-scale probing of paramagnetic centers location in nanodiamonds by ^{3}He NMR at low temperatures, *Phys. Chem. Chem. Phys.*, 2018, **20**, 1476–1484.

46 A. G. El-Deen, N. A. M. Barakat, K. A. Khalil and H. Y. Kim, Hollow carbon nanofibers as an effective electrode for brackish water desalination using the capacitive deionization process, *New J. Chem.*, 2014, **38**, 198–205.

47 V. B. Jaryal, A. Villa and N. Gupta, Metal-Free Carbon-Based Nanomaterials: Insights from Synthesis to Applications in Sustainable Catalysis, *ACS Sustainable Chem. Eng.*, 2023, **11**(41), 14841–14865.

48 S. P. Pattnaik, A. Behera, S. Martha, R. Acharya and K. Parida, Facile synthesis of exfoliated graphitic carbon nitride for photocatalytic degradation of ciprofloxacin under solar irradiation, *J. Mater. Sci.*, 2019, **54**, 5726–5742.

49 D. Fan, J. Feng, J. Liu, T. Gao, Z. Ye, M. Chen and X. Lv, Hexagonal boron nitride nanosheets exfoliated by sodium hypochlorite ball mill and their potential application in catalysis, *Ceram. Int.*, 2016, **42**, 7155–7163.

50 S. Yuan, B. Toury, S. Benayoun, R. Chiriac, F. Gombault, C. Journet and A. Brioude, Low-temperature synthesis of highly crystallized hexagonal boron nitride sheets with Li_3N as additive agent, *Eur. J. Inorg. Chem.*, 2014, 5507–5513.

51 R. Atchudan, T. N. J. I. Edison, S. Perumal and Y. R. Lee, Green synthesis of nitrogen-doped graphitic carbon sheets with use of Prunus persica for supercapacitor applications, *Appl. Surf. Sci.*, 2017, **393**, 276–286.

52 N. Kumar, R. Gusain, M. Masukume and S. S. Ray, B_2O_3-Nanoparticles-Decorated N-Rich Reduced Graphene Oxide Composites for the Enhanced Visible-Light-Assisted Photocatalytic Degradation of Ciprofloxacin, *Solar RRL*, 2023, **7**, 2300475.

53 F. Yang, C. Chi, C. Wang, Y. Wang and Y. Li, High graphite N content in nitrogen-doped graphene as an efficient metal-free catalyst for reduction of nitroarenes in water, *Green Chem.*, 2016, **18**, 4254–4262.

54 H. Kabir, H. Zhu, J. May, K. Hamal, Y. Kan, T. Williams, E. Echeverria, D. N. McIlroy, D. Estrada, P. H. Davis, T. Pandhi, K. Yocham, K. Higginbotham, A. Clearfield and I. F. Cheng, The sp^2–sp^3 carbon hybridization content of nanocrystalline graphite from pyrolyzed vegetable oil, comparison of electrochemistry and physical properties with other carbon forms and allotropes, *Carbon*, 2019, **144**, 831–840.

55 A. C. Popescu, G. E. Stan, L. Duta, C. Nita, C. Popescu, V. A. Surdu, M. A. Husanu, B. Bita, R. Ghisleni, C. Himcinschi and V. Craciun, The role of ambient gas and pressure on the structuring of hard diamond-like carbon films synthesized by pulsed laser deposition, *Materials*, 2015, **8**, 3284–3305.

56 A. Soni, D. Singh and N. Gupta, Heterogenization of Ionic Liquid on Multiwalled Carbon Nanotubes for Lead(II) Ion Detection, *ChemPlusChem*, 2024, e202400284.

57 M. A. Bajada, G. Di Liberto, S. Tosoni, V. Ruta, L. Mino, N. Allasia, A. Sivo, G. Pacchioni and G. Vilé, Light-driven C–O coupling of carboxylic acids and alkyl halides over a Ni single-atom catalyst, *Nat. Synth.*, 2023, **2**, 1092–1103.
58 V. Ruta, G. Di Liberto, F. Moriggi, Y. P. Ivanov, G. Divitini, G. Bussetti, V. Barbera, M. A. Bajada, M. Galimberti, G. Pacchioni and G. Vilé, Copper Single Atoms Chelated on Ligand-Modified Carbon for Ullmann-type C–O Coupling, *ChemSusChem*, 2024, **17**, e202301529.
59 J. Carrasco, A. Hodgson and A. Michaelides, A molecular perspective of water at metal interfaces, *Nat. Mater.*, 2012, **11**, 667–674.
60 O. Björneholm, M. H. Hansen, A. Hodgson, L.-M. Liu, D. T. Limmer, A. Michaelides, P. Pedevilla, J. Rossmeisl, H. Shen, G. Tocci, E. Tyrode, M.-M. Walz, J. Werner and H. Bluhm, Water at Interfaces, *Chem. Rev.*, 2016, **116**, 7698–7726.
61 Z. Guo, F. Ambrosio, W. Chen, P. Gono and A. Pasquarello, Alignment of Redox Levels at Semiconductor–Water Interfaces, *Chem. Mater.*, 2018, **30**, 94–111.
62 G. Di Liberto and L. Giordano, Role of solvation model on the stability of oxygenates on Pt(111): a comparison between microsolvation, extended bilayer, and extended metal/water interface, *Electrochem. Sci. Adv.*, 2024, **2**, e2100204.
63 E. Cancès, B. Mennucci and J. Tomasi, A new integral equation formalism for the polarizable continuum model: theoretical background and applications to isotropic and anisotropic dielectrics, *J. Chem. Phys.*, 1997, **107**, 3032–3041.
64 J. Tomasi, B. Mennucci and R. Cammi, Quantum Mechanical Continuum Solvation Models, *Chem. Rev.*, 2005, **105**, 2999–3094.